Acta Materialia 96 (2015) 249–257

Contents lists available at ScienceDirect

Acta Materialia

journal homepage: www.elsevier.com/locate/actamat

⟨a⟩ Prismatic, ⟨a⟩ basal, and ⟨c+a⟩ slip strengths of commercially pure Zr by micro-cantilever tests

Jicheng Gong [a,*], T. Benjamin Britton [b], Mitchell A. Cuddihy [b], Fionn P.E. Dunne [b], Angus J. Wilkinson [a]

[a] Department of Materials, University of Oxford, Parks Road, Oxford OX1 3PH, UK
[b] Department of Materials, Imperial College London, Exhibition Road, London SW7 2AZ, UK

ARTICLE INFO

Article history:
Received 21 February 2015
Revised 4 May 2015
Accepted 8 June 2015
Available online 24 June 2015

Keywords:
Zirconium
Micro-cantilever test
Slip properties
Anisotropy
CRSS

ABSTRACT

Slip strengths of ⟨a⟩ basal, ⟨a⟩ prism, and ⟨c+a⟩ pyramidal systems in commercially pure zirconium have been determined using micro-cantilever testing. A range of single crystal cantilevers 0.5 μm to 10 μm wide, oriented for single slip were prepared using focused ion beam (FIB) machining and subsequently deflected using a nanoindenter. The critical resolved shear stress (τ_{crss}) was found by fitting a crystal plasticity finite element model to the experimental load–displacement data for these micro-bending tests. All the three slip systems in α-Zr show a marked size effect in bending described well by $\tau_{CRSS}(W) = \tau_0 + AW^n$, where W is the cantilever width, τ_0 is the CRSS at the macro scale and $n = \sim -1$. The exponent, n, of near -1 is in good accord with hardening caused by the back stress generated by dislocations piling up at a diffuse barrier caused by the reduction of stress near the neutral axis. The macro scale CRSS values were used to successfully simulate deformation of a conventional macroscopic compression test.

1. Introduction

Zirconium is widely used in the nuclear industry as nuclear fuel rod cladding in water reactors, due to its low neutron cross section, good corrosion resistance and reasonable mechanical properties. To provide an adequate safety case and ensure safety during operation and shutdown, the mechanical performance of these polycrystalline components must be well known. Zirconium alloys for this application typically contain predominately the α-Zr (hcp) phase which exhibits pronounced anisotropy in both its elastic and plastic properties at the single crystal level. During processing strong and complex crystallographic textures are generated [1–3] which result in macroscopically anisotropic mechanical properties. Design and operation of a reactor must involve selection of appropriate materials, processing routes and textures to provide adequate strength for in-service operation. One such property is the critical resolved shear stress (CRSS) which describes the critical stress for plastic deformation to occur on a given slip system.

A physical understanding of conditions required for crystallographic slip is of clear importance when discussing the processes involved in deforming a polycrystalline aggregate. Unfortunately the reverse problem, extracting these physical properties from macroscopic tests is difficult due to competition between externally applied stresses and local constraint, due to networks of grains and other microstructural features which must deform together in order to accommodate plasticity. This problem is especially exacerbated when there are many 'soft' grains (i.e. ⟨c⟩ axis perpendicular to applied stress) which deform extensively while neighbouring 'hard' grains (⟨c⟩ axis parallel to applied stress) develop higher stresses but limited plastic strains. In these situations there is strong heterogeneity in the stress and plastic strain fields at the granular and intra-granular length scales. This heterogeneity or strain localisation has a significant role on the early stages of material failure processes.

The most direct route to determining CRSS values is to grow large single crystals that can be oriented so as to preferentially slip on the desired slip system during conventional tensile or compressive testing. This is a technically difficult undertaking especially for alloys and most results are from quite early work and are limited to pure Zr. In an extensive testing campaign Soo and Higgins [4] used strain rate jump tests to study the effects of oxygen content and temperature on the plastic flow of α-Zr oriented for prism slip. Near room temperature they found that increasing the oxygen content from 135 ppm to 2000 ppm caused the CRSS to increase from ~24 MPa to ~120 MPa, with a corresponding decrease in the activation volume from $312b^3$ to $40b^3$. Akhtar and Teghtsoonian [5] also made CRSS measurements for prism slip in high purity 100–200 ppm oxygen Zr single crystals. Further measurements on samples oriented for basal slip [6] were only able to generate CRSS values above ~850 K since at temperatures

* Corresponding author.

http://dx.doi.org/10.1016/j.actamat.2015.06.020
1359-6454/© 2015 Acta Materialia Inc. Published by Elsevier Ltd.

below this slip on prism planes or deformation twining was prevalent before activation of basal slip. At this low oxygen content the CRSS for basal slip was only slightly larger than for prism slip at temperatures above 1000 K but the CRSS increased on lowering temperature much more significantly for basal slip than prism slip so that basal slip was twice as hard as prism slip at ~900 K and the divergence continued to lower temperatures. Akhtar also conducted compression tests of ⟨c⟩ axis aligned Zr single crystals and obtained much higher CRSS values for ⟨c+a⟩ pyramidal slip while using slip traces to establish the slip plane was $\{10\bar{1}1\}$. Growing large single crystals for alloys is rarely possible and alternative strategies in which a combination of mechanical testing of a polycrystal while recording X-ray or neutron diffraction patterns coupled with modelling has typically been adopted. For example Skippon et al. [7] use a genetic algorithm to fit a Voce hardening law to neutron diffraction data obtained for in situ compression testing along different macroscopic axes of highly textured Zircaloy-2 alloy. The validity of the material property parameters obtained is dependent on the fidelity of the simulation used to model the deformation process.

Developments in focussed ion beam machining and micro-mechanical testing offer unique insight into deformation processes, as this approach enables micron and sub-micron scale single crystal specimens to be readily fabricated from polycrystalline samples. Unfortunately significant physical issues exist with testing on the small scale, as often the physics of local boundary conditions (i.e. high strain gradients [8,9]) and the scarcity of dislocation sources lead to increased strength and stochastic plastic flow [10]. This makes careful extraction of the properties more difficult, but provided adequate testing is performed and the physical basis of the size effect is understood then this is clearly possible [11–13]. Previously, we have implemented micro-cantilever tests to investigate the anisotropic elastic [14] and plastic properties [15] of titanium single crystals and devised suitable modelling routes for back calculation of key mechanical constants. In this study, we applied the method to study slip properties of single crystal commercially pure α-Zr. ⟨a⟩ Prismatic, ⟨a⟩ basal and ⟨c+a⟩ 1st order pyramidal slip systems were selectively activated in various sizes of micro-cantilevers. Crystal plasticity finite element analysis (CP-FEA) procedures were developed to extract CRSS values for different slip systems from the micro-tests. The size effect in micro-cantilever tests was determined for all the three slip systems. CRSS values extrapolated to the bulk were extracted by subtracting the size effect terms. These bulk CRSS values were then used within a CP-FEA simulation to predict the stress–strain response of a polycrystal deformed in compression, which was found to be in good agreement with experiment.

2. Experiments

A large bar of commercially pure Zr (99.2 wt.%) was purchased from Goodfellow (Goodfellow Cambridge Ltd, http://www.goodfellow.com). The specific chemical composition is given in Table 1. This material was heated to 750 °C, which is just below the α/β transus temperature, for 24 h in a vacuum furnace and then furnace cooled to grow grains, reduce defect populations and relieve residual stresses. After the annealing, the grain size increased to ~70 μm as shown in Fig. 1a. Micro-cantilevers were prepared within single Zr grains using focussed ion beam (FIB) machining.

Table 1
Chemical composition of the commercially pure Zr sample.

Zr	C (ppm)	Hf (ppm)	Fe (ppm)	Cr (ppm)	N (ppm)	O (ppm)	H (ppm)
Balance	250	2500	200	200	100	1000	10

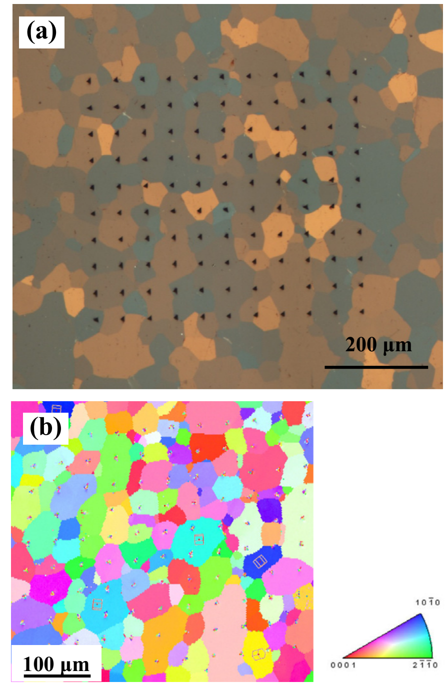

Fig. 1. (a) Polarised light optical image of Commercial pure Zr with indentation marks (b) crystal orientation map of the area shown in (a) indicating the orientation of the crystal with respect to the surface normal.

An indentation array was made to mark the area of interest. Cantilevers were fabricated far enough away from indents to exclude any residual effects associated with the indented volume. EBSD mapping was performed to characterise the local grain orientations, as shown in Fig. 1b. Individual grains, selected for single slip orientations, were chosen from EBSD grain orientation maps such as those in Fig. 1a and b.

Micro-cantilevers were prepared on a Zeiss NVison 40 dual beam FIB system, using a final step of 40 pA at 30 kV to minimize the FIB damage. All cantilevers tested in this work have triangular cross-section, which provides the flexibility to prepare micro-testing pieces in an arbitrary grain with the long axis of the beam pointing in any direction with the sample surface plane (i.e. two degrees of freedom). A series of tests were performed for each slip system with cantilever widths ranging from 0.5 μm to 10 μm. Care was taken to maintain the cantilever beam length to cantilever beam width ratio at 6:1 and to maintain this aspect ratio for all beam sizes. The 6:1 ratio was used so that the beams were neither too short to deviate strongly from simple beam theory [16] but nor were they too long so as to require prohibitive time for FIB machining. Fig. 2a is an example of 5 μm wide, 30 μm long micro-cantilever. Cantilever beam dimensions were carefully measured using the FEG SEM column of the NVision instrument.

Hexagonal materials have a number of slip systems, and there is considerable anisotropy in the single crystal plastic behaviour. Selective activation of each slip system was achieved by testing particular crystal orientations and micro-cantilever alignments within the α-Zr grains [15]. The basic rule for such a test is to maximise the Schmidt factor on the target slip system while minimizing the resolved shear stress for all the others. The precise geometry adopted for each slip system was as follows:

2.1. ⟨a⟩ type

$\langle 11\bar{2}0\rangle\{10\bar{1}0\}$ – prismatic slip: micro-cantilevers were prepared with the ⟨c⟩ axis in the surface plane perpendicular to the

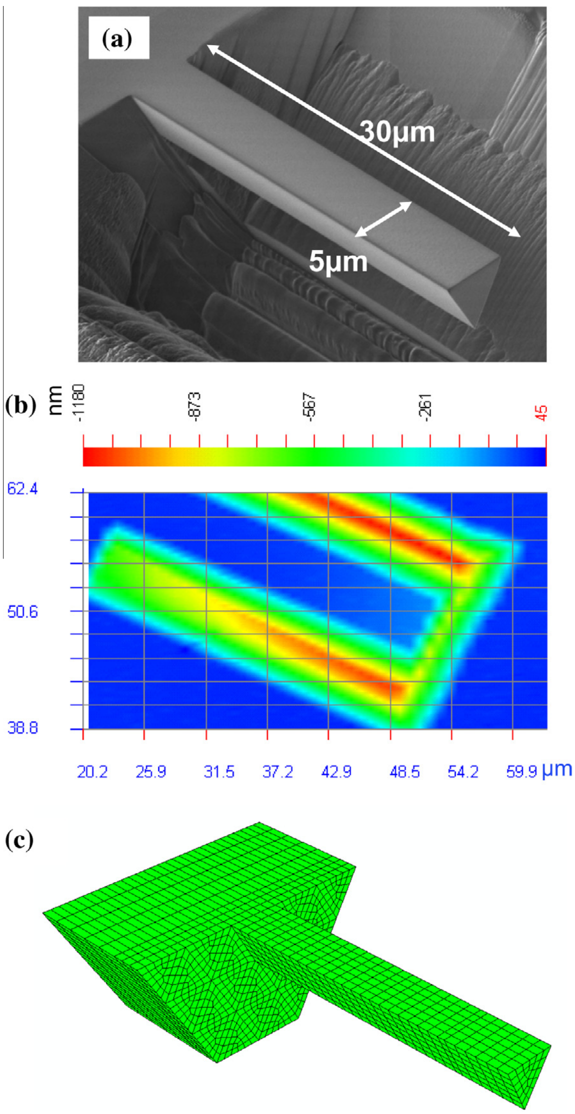

Fig. 2. (a) An example of 5 µm wide, 30 µm long cantilever with the triangular cross-section; (b) an AFM scan image of a 5 µm wide cantilever; and (c) finite element model geometry, showing built in end.

cantilever length with a prismatic plane at 45° to the cantilever axis (Fig. 3a). Schmidt factor for the selected ⟨a⟩ prism system is 0.5 (and the next highest, also an ⟨a⟩ prism system, is 0.25).

$\langle 11\bar{2}0\rangle\{0001\}$ – basal slip: The basal plane and one ⟨a⟩ direction were at 45° from the beam's length direction (Fig. 3b). Schmidt factor for ⟨a⟩ basal is 0.5 (and the next highest, an ⟨a⟩ prism system, is 0.25).

2.2. ⟨c+a⟩ type

$1/3\langle 11\bar{2}3\rangle$ $\{10\bar{1}1\}$ – 1st order pyramidal: The long axis of the cantilever was along the ⟨c⟩ direction with an ⟨a⟩ direction perpendicular to it within the surface plane. The ⟨c+a⟩ slip direction and slip plane is not 45° from the beam's length direction yet have the highest Schmidt factor of 0.40 while the resolved stress for the other ⟨a⟩ type slip systems is zero. The precise activation of 1st order pyramidal slip was confirmed after the test with slip line trace analysis.

The bulk sample was transferred to a nanoindenter platform for testing of each cantilever in turn. An Agilent G200 nanoindenter was used with the high resolution Dynamic Contact Module 2 head, which has a load and displacement resolution better than 0.1 µN and 0.1 nm, respectively. This nanoindenter system operates principally in load control, however with a fast feedback loop it was operated in a pseudo-constant displacement rate mode. This displacement rate was varied with cantilever size so as to obtain the same maximum strain rate of $\sim 5 \times 10^{-4}\ \mathrm{s}^{-1}$ for all cantilever sizes. Precise load point location was achieved by using pseudo-AFM imaging with a piezo nano-positioning stage and the indenter tip as the contact probe which was kept at a constant load of 0.5 µN. Fig. 2b is an example AFM image of a 5 µm wide cantilever.

For comparison compression tests were also undertaken on bulk polycrystalline samples measuring 2 mm in cross-section and 4 mm long. These were tested at a quasi-static strain rate of $5 \times 10^{-4}\ \mathrm{s}^{-1}$, which matches the maximum strain rate that occurs in the spatially varying strain field of the micro-cantilever tests. Strain was determined from the displacement of the cross-head after a correction for the compliance of the load frame and compression rig. The stress–strain response from the compression test was compared to CP-FEA simulations undertaken using CRSS data obtained from the micro-cantilever tests, and texture from EBSD measurements of a representative area.

3. Crystal plasticity finite element modelling

To extract the properties of each slip system, a crystal plasticity finite element model (Fig. 2c) was built to simulate the bending behaviour of a beam in the tested crystal orientation. The model was constructed such that the cantilever size, boundary and loading conditions match the experimentally made cantilevers. A bulk volume is attached to the root of the cantilever to capture the behaviour of the 'substrate' near the fixed end as an accurate boundary condition. The size of this volume was optimised to capture bulk effects in the minimum computational time and to accurately represent the experiment. In practise, a calibration step was performed whereby the size of the bulk region was increased until there were no significant changes in mechanical response of the model.

The constitutive equation is from Dunne's physically-based crystal plasticity modelling [17,18] in which the slip rates on individual slip systems are summed to give the local plastic velocity gradient $\mathbf{L}^{\boldsymbol{p}}$:

$$\mathbf{L}^p = \sum_j \rho b^2 v \exp\left(\frac{-\Delta F}{k_B T}\right) \sinh\left(\frac{(\tau^j - \tau_c^j)\Delta V}{k_B T}\right) \mathbf{s}^j \otimes \mathbf{n}^j, \quad (1)$$

where ρ is the density of gliding dislocations, b is the magnitude of the Burgers vector, v is the jump attempt frequency of dislocations trying to pass energy barriers, k_B the Boltzmann constant, T the absolute temperature, ΔF the Helmholtz free energy, ΔV the activation volume, $\boldsymbol{s}^{\boldsymbol{j}}$ the unit slip direction and $\boldsymbol{n}^{\boldsymbol{j}}$ the unit normal to the slip plane of the jth slip system which has a CRSS of τ_c^j, and is under a shear stress of τ^j. In all sizes of the micro-cantilever tests, the maximum strain rate is $\sim 5 \times 10^{-4}\ \mathrm{s}^{-1}$; this occurs at the bottom of the cantilever near the built-in end. At this relatively slow strain rate the flow stress of Zr is relatively insensitive to the strain rate at room temperature [19,20], and leaves τ_c^j as the single material parameter to be determined. Although relatively irrelevant to the CRSS values determined, care was taken to choose and check the parameters , v, ΔF and ΔV for the constitutive equation. For instance, according to Akhtar's work [5,6] the activation volume ranges from $55b^3$ to $80b^3$ for 1000 ppm oxygen for Zr in ⟨a⟩ prism slip while for ⟨c+a⟩ slip the results are not so clear but suggest a much smaller activation volume. The present simulations were run at both $13b^3$ and $80b^3$ for ΔV but this only generates a change of less than 1 MPa in the best fit ⟨a⟩ prism CRSS value. Table 2 lists

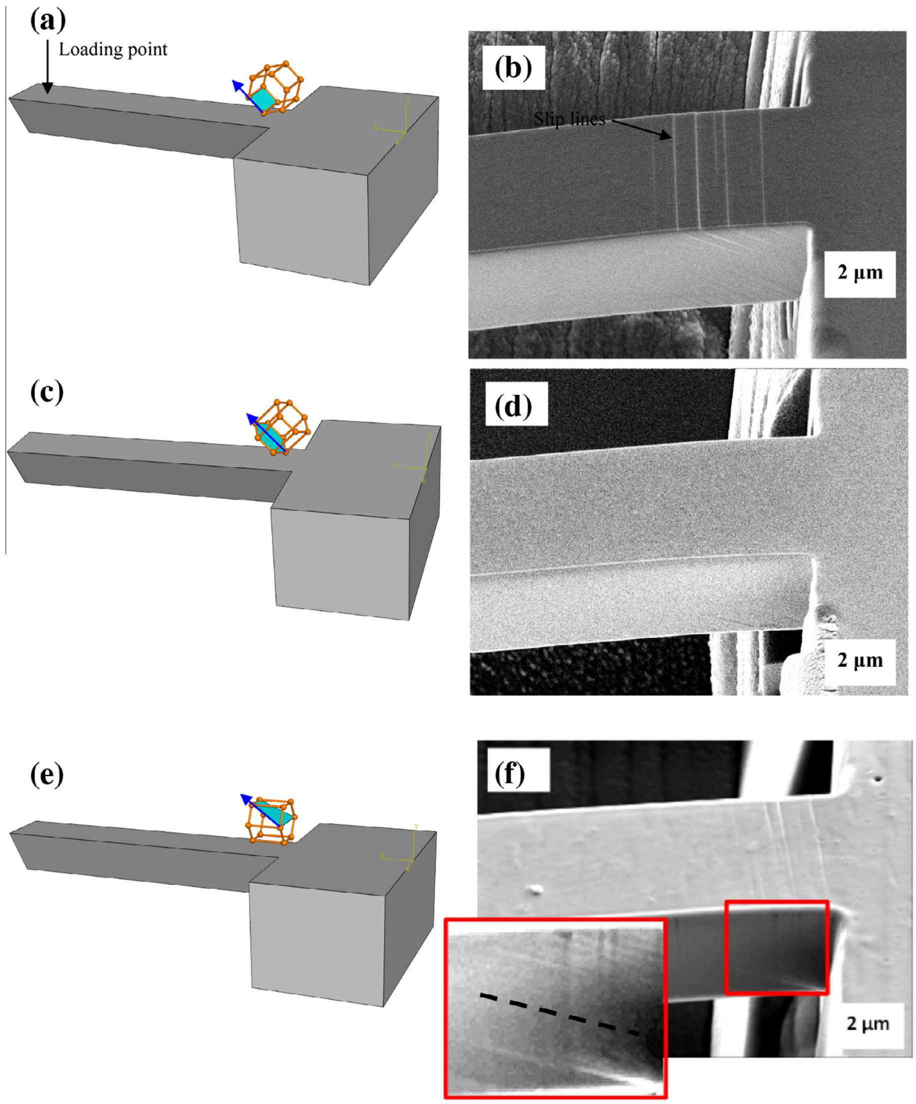

Fig. 3. Crystal orientation of (a) ⟨a⟩ prismatic; (c) ⟨a⟩ basal; and (e) ⟨c+a⟩ micro-cantilevers. A close-up view of deflected (b) 5 μm wide ⟨a⟩ prismatic; (d) 5 μm wide ⟨a⟩ basal; and (e) 2 μm wide ⟨c+a⟩ pyramidal beams (with inset showing features on side wall and dashed line indicating the expected alignment of the trace of first order pyramidal slip plane).

all the parameters for Eq. (1). The CRSS values τ_c^j are determined by a reverse process of fitting the model response to the experimental load–displacement data of the beams as has been described in [15].

In triangular micro-cantilevers, the bottom side of a beam develops larger stresses and is the first to yield. To extract the compressive CRSS, we limited the fitting process to small deflections where plastic strain is limited to the lower (compressive) part of the beam.

Besides CRSS, the elastic modulus along the length axis of a cantilever can be extracted in the FE model by fitting the initial slope of the load–displacement curves. The method to measure anisotropic elastic properties of hcp crystals using micro-cantilevers was detailed in [14].

A CP-FEA simulation was also used to predict the compression behaviour of a polycrystalline test piece using the same constitutive law in ABAQUS, implemented using a user element sub-routine (UEL). The model used consisted of a simple cubic array of 729 reduced quadratic elements (20 node hexahedral) with periodic boundary conditions. All these elements are 70 μm cubic unit, the dimensions of which match the grain size of macro commercially pure Zr. Each element was ascribed a different grain orientation selected from a list generated using experimental EBSD measurements. The constitutive law described by Eq. (1) was used with the parameter values given in Table 2 and CRSS values obtained directly from the micro-cantilever results extrapolated to bulk size (i.e. τ_0 from the micro-cantilever scaling law).

Table 2
Constants for the constitutive equation.

ρ (m^{-2})	b (m)	v (/s)	ΔF (J)	ΔV
1.0×10^{10}	3.2×10^{-10}	5.0×10^{19}	11.2×10^{-20}	$13b^3$

4. Results

4.1. ⟨a⟩ prismatic slip system

Three 5 μm wide ⟨a⟩ prismatic cantilevers were tested to a maximum displacement of 4 μm at a constant displacement rate of 20 nm/s (maximum strain rate $\sim 5 \times 10^{-4}$ s^{-1}). The indenter was brought into contact 27 μm from the built-in end, and in the middle of the beam's width. The load–displacement responses of one beam are shown as the green curves in Fig. 4. There is clearly a yielding response at ~1 μm defection after which the curve tends to become flat. Before the yielding, the beam has the linear response, corresponding to the elastic deformation, which can be used to assess Young's modulus in the beam length axis direction by fitting the slope at the initial elastic deflection period [14]. The elastic modulus of α-Zr in the tested $\langle 11\bar{2}0\rangle$ direction was determined to be 95 ± 6 GPa (with the error being the standard deviation of three measurements), which has a good agreement with the single crystal data of various experimental measurements of 98 GPa [21], 117 GPa [22] and theoretical calculation of 95 GPa [23], 122 GPa [24]. These elastic modulus results demonstrate that micro-cantilever tests are accurate.

Fig. 3b shows a close-up view of a deflected 5 μm wide beam, revealing substantial amounts of plasticity towards the built-in end. The alignment of slip bands on both the top and side surfaces confirms that the slip steps formed are due to the targeted ⟨a⟩ prism slip inclined at 45° to the top free surface.

In the deflection process of a micro-cantilever, stresses concentrate towards the built-in end of the beam. The top and bottom sides of the built-in area have tensile and compressive stress along the beam length direction, respectively. There is a neutral plane where the longitudinal stress is zero, which is a third of the thickness from the top surface for this triangular cantilever cross section. There is clear evidence shown in Fig. 3b that slip developed separately on either side of the neutral axis. Due to the triangular cross section, the stresses in the compression region are larger than the tensile region and therefore plasticity occurs first on the underside of the beam (compressive region). The onset of plastic deformation in the tensile part of the beam thus occurs only after considerable deflection of the cantilever and originates from sources near the top surface where the tensile stress is greatest.

For these ⟨a⟩ prismatic cantilevers the slip features seen on the side surfaces reduce in intensity from the outer (top and bottom) parts of the cantilever as the neutral plane is approached (indicating the presence of local strain gradients). Similar observations were made in ⟨a⟩ basal and ⟨c+a⟩ cantilevers.

Due to the heterogeneous nature of the bending behaviour, especially when coupled with the stochastic nature of slip on the small scale, it is difficult to directly assess the yield point on these load–displacement curves. Instead we use crystal plasticity FEM to simulate the bending behaviour of a micro-cantilever, and used a reverse fitting method for the load–displacement curves to extract slip properties.

The best fit of the CP-FEA simulations for these 5 μm wide ⟨a⟩ prismatic beams is also shown in Fig. 4 (pink curves) which fits the experimental data well. These simulations necessarily smooth

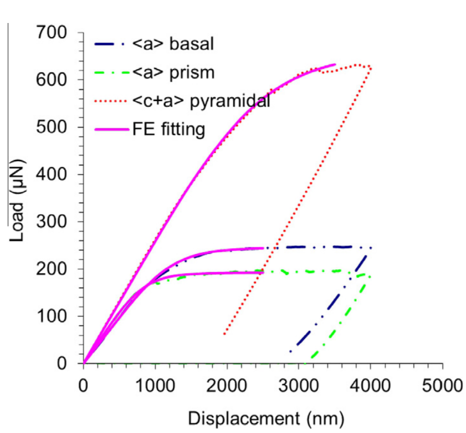

Fig. 4. Load displacement curves of 5 μm wide ⟨a⟩ prismatic (green), ⟨a⟩ basal (blue) and ⟨c+a⟩ pyramidal (red) cantilevers along with the best crystal plasticity finite element fitting curves (pink). (For interpretation of the references to colour in this figure legend, the reader is referred to the web version of this article.)

out the discrete nature of plasticity at the small scale. The average CRSS value obtained from the simulations is 206 ± 20 MPa for the 5 μm ⟨a⟩ prismatic case where the error is the standard deviation of the three measurements as indicated in Table 3.

Fig. 5 shows load–displacement data for ⟨a⟩ prismatic cantilevers of different widths, cut within similar grains selected to activate ⟨a⟩ prismatic slip (shown in Fig. 3a). The maximum deflection and deflection rate were scaled to match the maximum applied strain and strain rates for all cantilever sizes (i.e. the displacement rate is 2 nm/s, 4 nm/s, 8 nm/s and 40 nm/s for 0.5 μm, 1 μm, 2 μm and 10 μm wide cantilevers respectively).

As expected the larger cantilevers require larger loads to deform and the small load fluctuations appear to be less pronounced for the largest cantilevers. Based upon macroscopic beam bending calculations, the yield load would be proportional to the square of the beam size, assuming the aspect ratio of the beam is kept constant. However the experimental curves in Fig. 5 obviously do not follow this behaviour. This has been demonstrated by taking the CRSS value obtained from the 5 μm wide cantilevers and calculating the equivalent load–displacement curves using the CP-FEA model for the 0.5 μm, 1 μm, 2 μm and 10 μm wide cantilevers. Use of the 5 μm CRSS results in an ~84% smaller yield load compared to the measured load–displacement curve for the 2 μm wide cantilever. There are also discrepancies between simple simulations of the loads using CRSS determined from the 5 μm wide cantilevers and the experimental data for the 0.5 μm, 1 μm and 10 μm wide cantilevers. Higher CRSS values are required to account for the load displacement curves for smaller cantilevers.

CRSS values extracted from the CP-FEA simulations are given in Table 3 and plotted as a function of micro-cantilever size in Fig. 6. Matching to each curve results in an obvious increase in the CRSS at smaller cantilever widths whereas no obvious change in elastic modulus was seen for all size of these cantilevers. Each cantilever was examined after testing and alignment of slip bands indicates that ⟨a⟩ prismatic slip systems were exclusively activated as expected.

4.2. ⟨a⟩ basal slip system

Tests were conducted to activate ⟨a⟩ basal slip with the loading conditions and strain rate matching those for the ⟨a⟩ prismatic case. Fig. 4 shows the experimental load–displacement data (blue curve) for a 5 μm beam along with the best fit FEA simulations (pink curves). The elastic fitting gives the average modulus of 90 GPa, which again is in good accord with the literature [21–24]. Comparing with the ⟨a⟩ prismatic of beams, the yield loads are slightly higher. CRSS values extracted from fitting the FEA simulations give an average value of 235 ± 9 MPa for two 5 μm wide ⟨a⟩ basal cantilevers (error encompassing the data range) compared to an average CRSS of 206 MPa for ⟨a⟩ prismatic ones (see Table 3). Fig. 3d shows the built-in area of one 5 μm wide beam after deflection. In contrast to the ⟨a⟩ prismatic slip systems slip bands are not readily observed within the tensile (top) region. However, slip bands are visible on the side surfaces, where their alignment fits activation of ⟨a⟩ slip on the basal plane.

⟨a⟩ basal cantilevers of different sizes (0.5 μm, 1 μm, 2 μm and 10 μm wide) were tested with the scaled displacement rate and load point conditions. Again the variation of load–displacement curves with beam size does not follow macroscopic engineering approaches for cantilever deflection. Fitting each tested cantilever independently reveals a similar '*smaller is stronger*' size effect in the CRSS values for ⟨a⟩ basal slip as was seen for prism slip. The CRSS data are presented in Table 3, and plotted against cantilever size in Fig. 6, where it is seen that ⟨a⟩ basal slip is consistently slightly harder than ⟨a⟩ prism slip.

Table 3
Critical resolved shear stress of ⟨a⟩ prismatic, ⟨a⟩ basal and ⟨c+a⟩ slip for commercially pure Zr micro-cantilever beams.

Sample type	⟨a⟩ prism			⟨a⟩ basal			⟨c+a⟩		
Size	CRSS (MPa)		No. beams	CRSS (MPa)		No. beams	CRSS (MPa)		No. beams
	Mean	Std dev		Mean	Std dev		Mean	Std dev	
0.5 μm	745	18	3	792		2	1306	35	4
1 μm	507	49	3	618		2	1050	12	4
2 μm	324	21	3	383		2	791	53	4
5 μm	206	20	3	235		2	575	36	3
10 μm	182	5	3	322		2	501	22	4

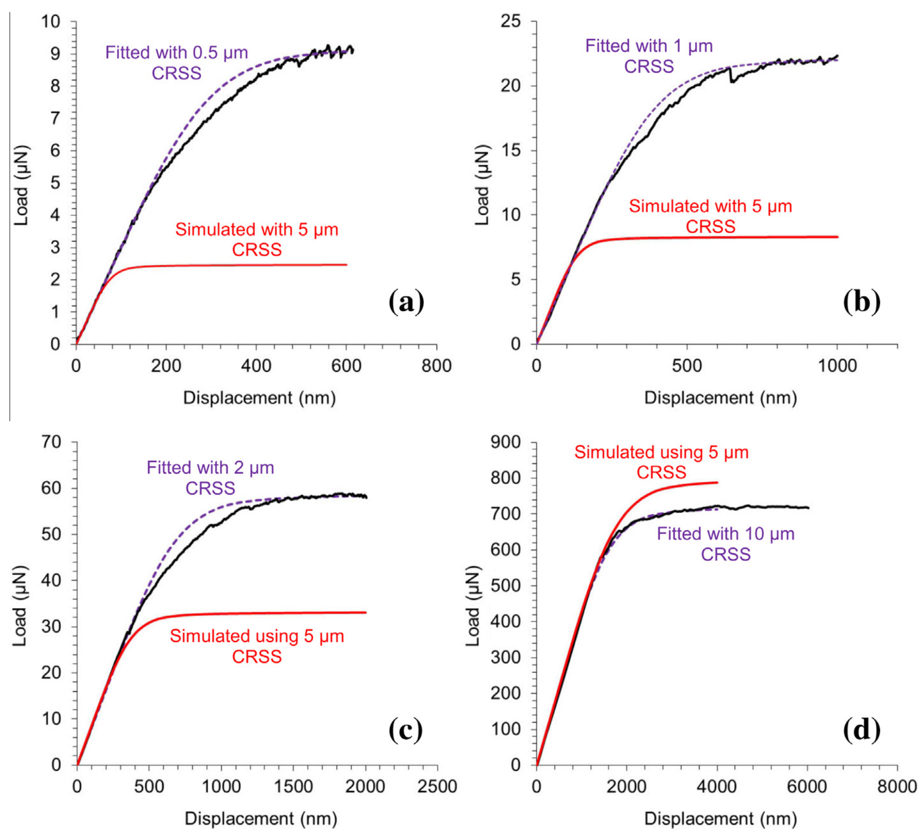

Fig. 5. Load–displacement curves for ⟨a⟩ prismatic cantilevers of different width: (a) 0.5 μm beam width; (b) 1 μm beam width; (c) 2 μm beam width; and 10 μm beam width. Thick black curves are the experimental results. The dash purple line is CP-FEA fitting for each size, respectively. The red curve is the simulation using CRSS from 5 μm ⟨a⟩ prismatic beams.

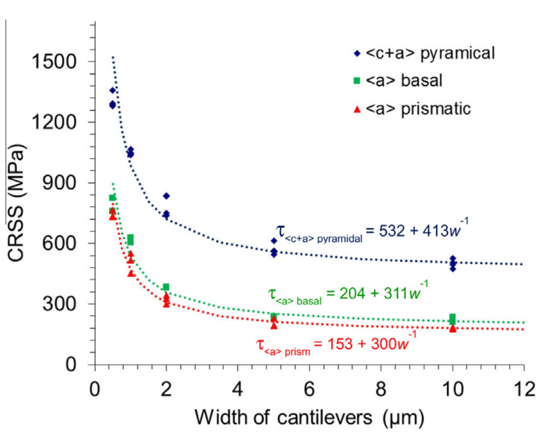

Fig. 6. CRSS vs. size (the beam width) for ⟨a⟩ prismatic, ⟨a⟩ basal and ⟨c+a⟩ commercially pure Zr cantilevers. Dash lines showing fit to $\tau_y = \tau_0 + Aw^{-1}$.

4.3. ⟨c+a⟩ slip system

The testing geometry has been selected to keep the resolved shear stress on ⟨a⟩ basal and ⟨a⟩ prismatic to be zero while applying shear stress to the ⟨c+a⟩ pyramidal slip system.

Load–displacement data for some 5 μm wide cantilevers are given in Fig. 4 (red curves), which also shows data for similarly sized ⟨a⟩ prismatic and ⟨a⟩ basal cantilevers for comparison. The pink lines show the best fit FEA simulations to the load–displacement data. The elastic modulus along ⟨c⟩ axis is determined to be 127 ± 8 GP based upon three beams. It can be seen that the yield load for these beams is ∼600 μN, which is considerably higher than the ⟨a⟩ prismatic and ⟨a⟩ basal beams (180–220 μN). The CRSS fitting for the first order ⟨c+a⟩ slip is 575 ± 36 MPa (with the error given from the standard deviation of three measurements) comparing with average values of 206 MPa and 235 MPa for ⟨a⟩ prismatic and ⟨a⟩ basal slip, respectively. In effect, these three testing geometries result in testing Zr with beam lengths orientated at

0°, 45° and 90° from the ⟨c⟩ axis and demonstrate significant plastic anisotropy in α-Zr.

Fig. 3f shows an SEM image of a ⟨c⟩ axis aligned micro-cantilever after testing and it can be seen that slip features are less marked than for the prism slip case (Fig 3b). Slip features on the top surface are observed to run perpendicular to the length of the cantilever which is consistent with either first order pyramidal planes $\{10\bar{1}1\}$, or basal planes $\{0001\}$, but inconsistent with either prism planes $\{10\bar{1}0\}$ for which slip features would be expected to run parallel to the length of the cantilever, or second order pyramidal $\{11\bar{2}1\}$ planes for which slip features should be inclined to the axis of the beam. The inset to Fig. 3f shows the inclined side face of the cantilever with contrast altered to better reveal slip features which are seen in both the compressive and tensile parts of the test piece. The alignment of the trace of first order pyramidal planes $\{10\bar{1}1\}$ on the image was calculated from knowledge of the sample tilt and crystallography and is shown by the dashed line in Fig. 3f to agree well with the observed features.

FEA simulations were again used to extract CRSS values from load–displacement curves obtained for the range of cantilever sizes. Consistent with previous examples a 'smaller is stronger' size effect was observed, however the difference appears less marked for this stronger cantilever orientation than it was for either ⟨a⟩ prismatic, or ⟨a⟩ basal slip. CRSS values determined by fitting simulations to experimental load–displacement data are given in Table 3 and plotted in Fig. 6.

4.4. Polycrystal compression behaviour

The stress–strain response determined for the macroscopic polycrystalline sample deformed in compression is shown in Fig. 7a. Simulations were undertaken using the CP-FEA modelling scheme described above. No attempt was made to properly capture the grain morphology and instead a cubic array of grains was used

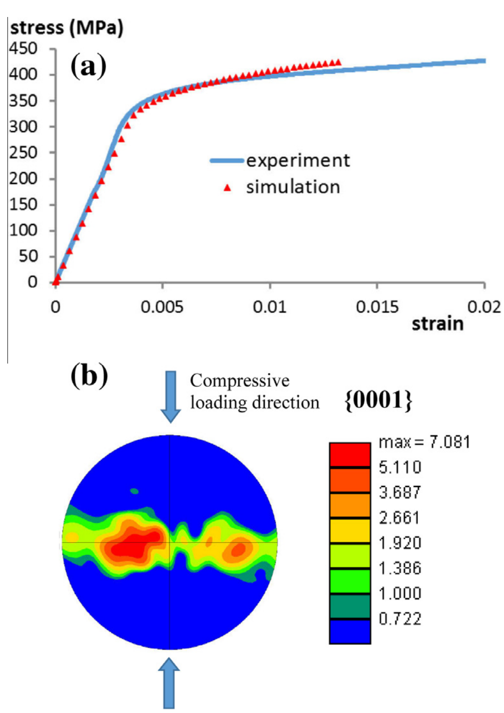

Fig. 7. (a) Experimentally determined stress–strain response of polycrystalline commercially pure Zr sample compared to CP-FEA simulation results using CRSS obtained from micro-cantilever data presented in Fig. 6 and extrapolated to bulk size. (b) $\{0001\}$ pole figure showing the compression axis indicating the texture measured by EBSD and used as input to the CP-FEA simulation.

with periodic boundary conditions, but the texture was taken directly from EBSD measurements of crystal orientation. The CRSS values in this model were based upon values extracted from Fig. 6, as extrapolated to bulk single crystals with: ⟨a⟩ prism 153 MPa, ⟨a⟩ basal 204 MPa, and ⟨c+a⟩ pyramidal 532 MPa. No adjustment was made to any other parameters in the constitutive law. The level of agreement between the simulation and experimental measurement is very good.

5. Discussion

This extensive study of all the slip systems in commercially pure α-Zr for micro-cantilever tests shows that there are a few factors to consider when trying to determine the engineering properties of materials using micro-mechanical testing. For all three slip systems '*smaller is stronger*' (Fig. 6). Cantilevers of smaller widths (and also lengths) have higher critically resolved shear stresses when analysed using the physically based crystal plasticity modelling route.

In addition to quantitative analysis of strength at the small scale, the nature of plasticity can be directly observed from the post-test slip lines. In particular, slip traces for ⟨a⟩ prismatic beams are clearly observed on the top tensile surface of the cantilevers whereas ⟨a⟩ basal ones do not show visible traces, consistent with prior work in Ti [15]. This indicates the difference is due to slip behaviour of the two systems in hexagonal materials. Akhtar [6] noted that basal slip features were wavy on the surfaces of large single crystals deformed in tension. Similar observations have been reported for Ti [25] and the wavy nature is associated with cross-slip onto the prism plane for which dissociation into partials is more favoured.

For ⟨c+a⟩ slip the slip trace analysis was consistent with slip on the $\{10\bar{1}1\}$ planes on both the tensile and compressive parts of the micro-cantilevers. On the lower compressive part of the cantilever the slip tended to be dominated by a larger band intersecting the point where the lower apex of the beam joined to the bulk of the sample, while on the tensile part deformation tended to be dispersed over more slip features of less intensity. Previous macroscopic testing has also identified $\{10\bar{1}1\}$ planes for ⟨c+a⟩ slip in Zr under both tension and compression loading with Akhtar [26] using slip trace analysis on single crystals compressed along ⟨c⟩ at temperatures in the range 800–1100 K while Numakura et al. [27] reported TEM analysis for ⟨c+a⟩ dislocations in polycrystalline Zr deformed in tension at room temperature. Tension–compression asymmetry of yielding has been reported for both Zr and Ti alloys eg [28–30] Jones & Hutchinson particularly associated asymmetry with ⟨c+a⟩ slip and recent TEM observations by Ding et al. [31] of Ti–6Al–4V micro-cantilevers deformed in ⟨c+a⟩ slip show significantly more cross-slip on the compressive side of the beam. The strains are larger in the compressive part of the beam and deformation here is thought to dominate the early stages of cantilever bending that have been used to extract the CRSS values reported.

The size effect data can be explored in significantly more detail, and 'smaller is stronger' has been seen previously in bending for titanium [32,33] and copper [34,35]. The physical basis of this effect, for the cantilever geometry, is the soft pile-up at the neutral axis, associated with the transition between a compressive lower portion of the beam to the tensile top face. A pile-up of dislocations at the neutral axis presents a back stress which inhibits further dislocation motion (and source activation) and therefore generates significant hardening. Our primary interest with this approach is extraction of macroscopically relevant mechanical properties, which can easily be inserted into design and lifing codes for reactor designs. The physics of this problem is also interesting and must be tackled to generate the 'macro' CRSS for models at the longer length-scale (though the presence of strain gradients, related to this issue are gaining significant traction in the modelling community when exploring weakest link failure modes, such as in dwell fatigue in Ti alloys [17,36]).

Our previous analysis of titanium data [33] indicated that the experimental data were well represented by a modification of the simple power law to include a size independent term τ_0 to represent the CRSS of a bulk single crystal:

$$\tau_y = \tau_0 + Aw^n, \tag{2}$$

Furthermore the exponent n was found to be -1.1 [32] for commercially pure Ti, and -1.14 for Cu bent to high surface strain by Motz et al. [12]. These exponent values are considerably higher than would be anticipated from using the GND density required to support the beam curvature within a Taylor hardening model which would lead to an exponent of -0.5. However, as is clearly evident in the post-test micrographs a Taylor hardening law arising from forest hardening is not applicable as these beams deform in a single slip mode and result in much more ordered slip (and a finite slip spacing). The deformed structures in these Zr micro-cantilevers more likely consist of dislocation arrays piling up towards the neutral axis where the low stresses provide a barrier to further slip as has been observed in TEM for similar Ti–6Al–4V cantilevers [31,37]. Motz et al. [12,38] have shown that the back stress generated by such dislocation pile-ups leads to an exponent of -1 which is in good accord with this (and other Ti [32], Cu [34]) experimental data. Recent simulations of micro-cantilever bending that couple discrete dislocation dynamics and FEA have been made by Tarleton et al. [39]. Comparison was made to some of the ⟨a⟩ prism micro-cantilever data presented here and the $n = -1$ size exponent was evident in the simulation results. Fig. 6 shows that the CRSS data extracted for all three slip systems are well represented by Eq. (2) with n forced to -1.

With the scaling exponent forced to -1, we find the constant A which represents the strength of the size effect to be 300 ± 30 Pa m for ⟨a⟩ prism, 311 ± 66 Pa m for ⟨a⟩ basal, 413 ± 55 Pa m for ⟨c+a⟩ slip, where the error bars indicate a 95% confidence interval. Although greater stress is required for the harder ⟨c+a⟩ slip test the extent of bending (i.e. deflection) is controlled by the number (and magnitude of Burgers vector) of dislocations within the pile-up. Hence for a given deflection of a beam of given dimensions the broadly similar dislocation density levels and back stresses are expected so that the physics is still consistent with an exponent of -1. The constant A however is modified somewhat by anisotropy of shear modulus and magnitude of the Burgers vector. The magnitude of the Burgers vector is 0.32 nm for the two ⟨a⟩ type slip systems for which A values are found to be similar and larger at 0.61 nm for ⟨c+a⟩ for which a larger A value is found. This suggests that Burgers vector length has a key impact in controlling the strength of the size effect in micro-bending tests.

Cantilevers were made with over a decade in size to enable extrapolation to bulk values with reasonable certainty and using fitting as presented in Fig. 6, the bulk CRSS values are 153 ± 30 MPa for the ⟨a⟩ prismatic, 204 ± 66 MPa for ⟨a⟩ basal, and 532 ± 58 MPa for the ⟨c+a⟩ slip, where errors indicate a 95% confidence interval. Fig. 6 shows as dashed lines that this procedure gives a good fit to the data.

The bulk ⟨a⟩ prismatic and ⟨a⟩ basal CRSS values determined here appear to be significantly higher than other values in the literature [4–7,40,41]. It is well known that CRSS is strongly dependant on alloy content (even in 'commercially pure systems') which makes direct comparisons difficult as changes at trace levels can cause significant differences. Fig. 8 compares the result obtained here for the CRSS of ⟨a⟩ prism slip with other values in the literature for Zr at different equivalent oxygen contents. The

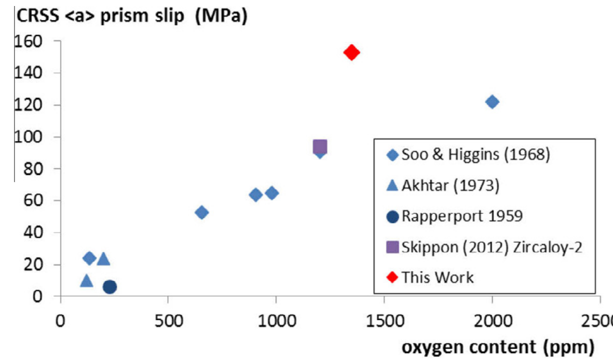

Fig. 8. Effect of oxygen equivalent concentration on CRSS value for ⟨a⟩ prism slip in commercially pure Zr, and zircaloy-2.

results obtained here are some ~50 MPa higher than expected from interpolation of values in the literature which forces a critical examination of why this should be so.

Testing at the small scale has some known concerns, including damage induced during sample manufacture where ion beam cutting (FIB damage) can introduce radiation defects and local hardening (e.g. in the strength of nano-pillar tests [42]). For our study, cantilevers are typically not 'nano' and a surface 'skin' of radiation damage a few tens of nanometers deep is considerably smaller than our micro-cantilevers of 0.5 μm to 10 μm wide with the 6:1 length-to-width ratio. Furthermore, when considered properly the strength of micro-cantilevers is size dependent and shows a significant deviation only at the smaller scale.

The constitutive law employed in the simulations used to extract the CRSS values contains no hardening term despite tests continuing to maximum strain levels of ~7.5%. Comparing the best fit simulation results to the experimental load–displacement data for the ⟨a⟩ prism and basal slip cases it is noticeable that the experiments deviate from linearity slightly earlier than the simulated curves (as shown in Figs. 4 and 5). The slight hardening present in the experimental data is thought to come from the gradual build-up of back stresses from the pile-ups which evolve during beam deflection but is not captured by the simulation. This is a more obvious effect for the smaller cantilever sizes, where the back stress from the pile up plays a larger role. The CRSS value used in the simulations is therefore likely to be increased to compensate for the lack of hardening while still capturing the saturation of the load–displacement data at the larger displacements when the pile-ups are more densely populated.

There is an agreement that ⟨a⟩ prismatic slip has the lowest CRSS, and therefore is most easy to be activated. By comparison to ⟨a⟩ prism slip the ⟨a⟩ basal slip has a CRSS that is only slightly (~33%) higher while for ⟨c+a⟩ slip the increase is very significant (~350%). This demonstrates the strong anisotropy in the single crystal behaviour of α-Zr. The ratio here is up to 3.5, which is in good agreement with other values in the literature of 2.6 [40] and 3.3 [41].

Although the CRSS for ⟨a⟩ prism slip seems elevated compared to other literature values when considering effective oxygen content it is clear that there is good consistency between the CRSS values obtained from the micro-cantilever tests and the bulk stress–strain response of a polycrystalline of the same material.

6. Conclusions

The ⟨a⟩ prism, ⟨a⟩ basal, and ⟨c+a⟩ on the first order pyramidal plane slip systems of commercial pure α-Zirconium were selectively investigated by testing particular crystal orientations using various sizes of micro-cantilever tests. Slip properties were determined by a reverse fitting approach based on a crystal plasticity finite element model. The macro CRSSs were extracted by extrapolation of the size effect data, using a simple scaling law based upon 1/width. The main results can be summarised as:

(1) For all slip systems the increase in CRSS τ with reducing cantilever width w is well represented by the model $\tau = \tau_0 + \frac{A}{w}$, τ_0 is the CRSS for an infinite sample and A is a constant reflecting the strength of the size effect. This model is well accounted for by the increased back stress generated by dislocations piling up at the neutral axis. The parameter A is larger for ⟨c+a⟩ slip for which the magnitude of the Burgers vector is also higher.
(2) ⟨a⟩ prismatic slip is the most easy slip system with the macro CRSS determined to be 153 ± 30 MPa (with ±30 MPa 95% confidence interval). Its size effect parameter A is 300 Pa m (with ±30 Pa m 95% confidence interval). Slip bands for this system are clear and the most planar among the three systems.
(3) For ⟨a⟩ slip on the basal plane a macro CRSS of 204 MPa (with ±66 MPa 95% confidence interval) was determined. This is~30% higher than for ⟨a⟩ slip on prism planes. The scaling parameter, A, of 311 Pa m (with ±63 Pa m 95% confidence interval) is comparable to that for ⟨a⟩ prismatic. No intense planar slip bands could be seen on the top surface of these beams suggesting that basal slip involves more cross-slip.
(4) Slip trace analysis showed that ⟨c+a⟩ slip occurred on first order pyramidal planes. The macro CRSS was determined to be 532 MPa (with ±58 MPa 95% confidence interval), a factor of 3.5 times harder than for ⟨a⟩ slip on prism planes. ⟨c+a⟩ slip also has the strongest size effect term with A being 413 Pa m (with ±55 Pa m 95% confidence interval), consistent with a scaling of A with Burgers vector.
(5) The CRSS values extracted from the micro-cantilever tests for the individual slip systems were used within a CP-FEA simulation of a polycrystal under compression. The agreement between the predicted stress–strain curve and that experimentally determined was extremely good adding confidence to the micro-cantilever test data.

Acknowledgements

We are grateful for financial support from the Engineering and Physical Sciences Research Council (grants EP/K039237/1, EP/H018921/1, EP/K034332/1). The research data supporting this paper will be made available on the Oxford Research Archive (http://ora.ox.ac.uk/) and can be link to using DOI:10.5287/bodleian:s4655h192. We thank Prof David Rugg (Rolls-Royce) and Prof Michael Preuss (Manchester) for insightful discussion and encouragement within the HexMat Programme, and Mr David Lloyd for assistance in preparing some of the Zr samples used in this work.

References

[1] E.K. Cerreta, J.P. Escobedo, P.A. Rigg, C.P. Trujillo, D.W. Brown, T.A. Sisneros, B. Clausen, M.F. Lopez, T. Lookman, C.A. Bronkhorst, F.L. Addessio, Acta Mater. 61 (2013) 7712.
[2] J.P. Escobedo, E.K. Cerreta, C.P. Trujillo, D.T. Martinez, R.A. Lebensohn, V.A. Webster, G.T. Gray, Acta Mater. 60 (2012) 4379–4392.
[3] H.R. Wenk, I. Lonardelli, D. Williams, Acta Mater. 52 (2004) 1899–1907.
[4] P. Soo, G.T. Higgins, Acta Metall. Mater. 16 (1968) 177–186.
[5] A. Akhtar, A. Teghtsoonian, Acta Metall. Mater. 19 (1971) 655–663.
[6] A. Akhtar, Acta Metall. Mater. 21 (1973) 1–11.
[7] T. Skippon, C. Mareau, M.R. Daymond, J. Appl. Crystallogr. 45 (2012) 627–643.
[8] E. Arzt, Acta Mater. 46 (1998) 5611–5626.
[9] D.Y.W. Yu, F. Spaepen, J. Appl. Phys. 95 (2004) 2991–2997.
[10] J.R. Greer, W.D. Nix, Phys. Rev. B 73 (2006) 245410.
[11] D. Di Maio, S.G. Roberts, J. Mater. Res. 20 (2005) 299–302.
[12] C. Motz, T. Schoberl, R. Pippan, Acta Mater. 53 (2005) 4269–4279.
[13] M.D. Uchic, D.M. Dimiduk, J.N. Florando, W.D. Nix, Science 305 (2004) 986–989.
[14] J.C. Gong, A. Wilkinson, Philos. Mag. Lett. 90 (2010) 503–512.
[15] J.C. Gong, A.J. Wilkinson, Acta Mater. 57 (2009) 5693–5705.
[16] D.E.J. Armstrong, A.J. Wilkinson, S.G. Roberts, J. Mater. Res. 24 (2009) 3268–3276.
[17] F.P.E. Dunne, A. Walker, D. Rugg, Proc. R. Soc. Math. Phys. Eng. Sci. 463 (2007) 1467–1489.
[18] F.P.E. Dunne, D. Rugg, A. Walker, Int. J. Plast. 23 (2007) 1061–1083.
[19] D. Lee, F. Zaverl, Acta Metall. Mater. 26 (1978) 1771–1780.
[20] V. Ramachan, R.E. Reedhill, Metall. Trans. 1 (1970) 2105–2109.
[21] E.S. Fisher, C.J. Renken, Phys. Rev. A 135 (1964) A482–A494.
[22] G. Simmons, H. Wang, Single Crystal Elastic Constants and Calculated Aggregate Properties, MIT Press, Cambridge, MA, 1971.
[23] G.J. Ackland, S.J. Wooding, D.J. Bacon, Philos. Mag. A 71 (1995) 553–565.
[24] Y. Udagawa, M. Yamaguchi, H. Abe, N. Sekimura, T. Fuketa, Acta Mater. 58 (2010) 3927–3938.
[25] A. Akhtar, Metall. Trans. A 6 (1975) 1105–1113.
[26] A. Akhtar, J. Nucl. Mater. 47 (1973) 79–86.
[27] H. Numakura, Y. Minonishi, M. Koiwa, Philos. Mag. A 63 (1991) 1077–1084.
[28] L.B. Addessio, E.K. Cerreta, G.T. Gray, Metall. Mater. Trans. A 36A (2005) 2893–2903.
[29] J.J. Fundenberger, M.J. Philippe, F. Wagner, C. Esling, Acta Mater. 45 (1997) 4041–4055.
[30] I.P. Jones, W.B. Hutchinson, Acta Metall. Mater. 29 (1981) 951–968.
[31] R.G. Ding, J.C. Gong, A.J. Wilkinson, I.P. Jones, Acta Mater. 76 (2014) 127–134.
[32] J.C. Gong, A.J. Wilkinson, Philos. Mag. 91 (2011) 1137–1149.
[33] J.C. Gong, A.J. Wilkinson, Acta Mater. 59 (2011) 5970–5981.
[34] D. Kiener, C. Motz, T. Schoberl, M. Jenko, G. Dehm, Adv. Eng. Mater. 8 (2006) 1119–1125.
[35] E. Demir, D. Raabe, F. Roters, Acta Mater. 58 (2010) 1876–1886.
[36] F.P.E. Dunne, R. Kiwanuka, A.J. Wilkinson, Proc. R. Soc. Math. Phys. Eng. Sci. 468 (2012) 2509–2531.
[37] R.G. Ding, J.C. Gong, A.J. Wilkinson, I.P. Jones, Philos. Mag. 92 (2012) 3290–3314.
[38] C. Motz, D. Weygand, J. Senger, P. Gumbsch, Acta Mater. 56 (2008) 1942–1955.
[39] E. Tarleton, D.S. Ballint, J.C. Gong, A.J. Wilkinson, Acta Mater. 88 (2015) 271–282.
[40] S. Cai, M.R. Daymond, R.A. Holt, Acta Mater. 57 (2009) 407–419.
[41] D. Gloaguen, J. Fajoui, E. Girard, R. Guillen, J. Appl. Crystallogr. 43 (2010) 890–899.
[42] S. Shim, H. Bei, M.K. Miller, G.M. Pharr, E.P. George, Acta Mater. 57 (2009) 503–510.